Article

Not peer-reviewed version

In Situ Synthesized Manganese Ferrite/Carbon Composite Nano-Material: A Novel Electrode Material for High-Performance Supercapacitors

Tshiamo Baloyi , Ndeye Fatou Diop , Rashed Ali Adam , Erence Nkuna , Gift Rutavi , Motlalepula Rebecca Mhlongo , Ncholu Manyala * , Vusani Muswa Maphiri *

Posted Date: 25 February 2026

doi: 10.20944/preprints202602.1493.v1

Keywords: in situ synthesis; $MnFe_2O_4$; supercapacitor; energy storage; composite

 doi:10.20944/preprints202602.1493.v1

Article

In Situ Synthesized Manganese Ferrite/Carbon Composite Nano-Material: A Novel Electrode Material for High-Performance Supercapacitors

Tshiamo Baloyi [1], Ndeye Fatou Diop [2], Rashed Ali Mohamed Adam [2], Erence Nkuna [2], Gift Rutavi [2], Motlalepula Rebecca Mhlongo [1], Ncholu Manyala [2,*] and Vusani Muswa Maphiri [1,*]

[1] Department of Physics, Sefako Makgatho Health Sciences University, Medunsa 0204, South Africa

[2] Department of Physics, University of Pretoria, Pretoria 0028, South Africa

* Correspondence: ncholu.manyala@up.ac.za (N.M.); vusanimuswamaphiri@gmail.com (V.M.M.)

Abstract

This study presents an in situ synthesis of a novel Manganese Ferrite/Carbon (MF/C) composite material via citrate sol–gel route followed by calcination in an inert argon (Ar) atmosphere. The structural and morphological and porosity properties were characterized using X-ray diffraction (XRD), Fourier transform infrared (FTIR) spectroscopy, scanning electron microscopy (SEM), Energy Dispersive X-ray Spectroscopy (EDX), and N_2 gas physisorption analysis. Electrochemical evaluation of the MF/C in 3M KOH electrolyte in a three – electrode configuration showed a high specific capacity of 39.26 mAh g^{-1} at 1 Ag^{-1} and a rate capability of 69% at 5 Ag^{-1} an equivalent series resistance (ESR) of 0.798 Ω. Subsequently, an asymmetric hybrid supercapacitor device (MF/C//AC) was fabricated using MF/C as the positive electrode and human derived activated carbon (AC) as the negative electrode. The assembled device exhibited remarkable performance with a wide operating voltage window of 1.4 V, a high sweeping potential of 1 V s^{-1}, a specific capacity, energy, power and maximum power of 42.4 $mAhg^{-1}$, 16.35Wh kg^{-1}, 1944W kg^{-1} and 236 kW kg^{-1}, respectively and excellent capacitance retention of 92% after 15,000 charge–discharge cycles. The in-situ preparation approach significantly reduced synthesis time and cost compared to conventional multi-step methods as less equipment were required, while still achieving comparable or superior electrochemical performance to other supercacitors in literature.

Keywords: in situ synthesis; $MnFe_2O_4$; supercapacitor; energy storage; composite

1. Introduction

To meet the world's growing energy demands, scientists have recently focused a great deal of attention on the development of environmentally friendly and sustainable energy storage and conversion technologies [1,2]. The need for effective sustainable energy transmission and storage around the world has led to a growing interest in supercapacitors among electrochemical energy storage devices [3]. In addition to being a desirable medium for storing renewable energy, supercapacitors can serve as an effective power source for portable electronic devices due to their high power density, high charge-discharge rate, and exceptional stability. Their effective applications include regenerative braking, emergency doors, system backup, and some automobiles as the primary power source [3,4].

Most widely utilized supercapacitors are pseudo/Faradic-capacitors, owing to their superior electrochemical performance compared to electric double-layer capacitors (EDLCs). Their enhanced performance is primarily due to the fast and reversible redox reactions, which contribute to higher specific capacity and energy [5]. Furthermore, aqueous supercapacitors offer higher power density, cycling stability, and more safety with lower cost, making them a more sustainable option than commercial lithium-ion batteries and sodium/potassium intercalation batteries, which typically use

 doi:10.20944/preprints202602.1493.v1

more expensive, flammable, and toxic materials. The choice of pseudocapacitors is to provide an intermediate state, where batteries and EDLCs typically fall short—by combining the high energy density of batteries with the quick discharge rates of EDLCs [6].

As a result of the limitations associated with current energy storage materials, several approaches have been employed to enhance the performance of pseudocapacitors. These include the synthesis of iron oxides with distinct structures, the production of multicomponent iron oxides, and the blending of carbon with iron oxides. The electrochemical characteristics of iron oxides can also be modified by introducing different metallic cations. Among these, manganese has attracted attention due to its multiple valence states, which facilitate redox reactions and improve conductivity and mechanical stability during discharge. Moreover, the possible synergistic interaction between manganese and iron may enhance the electrochemical activity of manganese ferrite ($MnFe_2O_4$)[1,7–9]. Our group has previously reported similarly such as $CoFe_2O_4$ [10]and $NiFe_2O_4$ [11] in supercapacitor application. $CoFe_2O_4$ based device showed an enhanced pseudocapacitive charge storage performance with a maximum specific capacitance and capacity values of 756.5 Fg^{-1} and 57.16 $mAhg^{-1}$. While $NiFe_2O_4$ based device demonstrated optimum electrochemical charge storage performance of specific capacitance and capacity values of 1128 Fg^{-1} and 58 $mAhg^{-1}$, respectively.

The inherent characteristics of $MnFe_2O_4$ make it a promising electrode material for energy storage applications [12,13]. Its distinct spinel structure promotes enhanced electrochemical activity by enabling numerous redox-active sites. Prior research has demonstrated that $Mnfe_2O_4$ can deliver strong electrochemical performance, including cyclic stability and good capacitance. However, challenges such as inadequate electronic conductivity and particle aggregation continue to limit its full potential [12–14]. To advance its application in supercapacitors, more research into the structural and electrochemical behaviour of $MnFe_2O_4$ as well as a deeper understanding of its charge storage mechanisms are required.

Despite considerable progress in material design, the most commonly employed synthesis approaches remain conventional multi-step methods. Typically, these involve first preparing the metal oxide using techniques such as sol-gel, hydrothermal, solvothermal, or auto-combustion, then annealing in air [15–18]. Simultaneously, carbon-based materials are often synthesized separately through processes such as carbonization/activation [19–21], chemical vapor deposition (CVD) [22,23], Hummers' method [24,25], or arc discharge [26]. The two components are then combined into a composite using methods like hydrothermal treatment [27] or ball milling [28]. These multi-step procedures are often time-consuming, require numerous chemicals, and demand a wide range of specialized equipment, increasing production cost and complexity.

In contrast, this work adopts a simplified in situ sol-gel and calcination method, where the dried gel from sol-gel precursor is directly calcined in an inert argon (Ar) atmosphere. This approach not only promotes effective dispersion of the metal oxide within the carbon matrix but also significantly reduces the number of synthesis steps, material and equipment's requirements, and the overall cost. Additionally, the method offers improved simplicity and scalability, making it suitable for practical and large-scale applications. Moreover, the MF/C electroactive material prepared using this novel method yielded electrochemical results comparable to those reported in literature using more complex and resource-intensive techniques [18,29,30] ,further validating the efficiency and potential of this in situ strategy.

2. Experimental Details

2.1. Materials Used

Manganese chloride tetrahydrate ($MnCl_2{\cdot}4H_2O$, 98%), Iron (III) chloride hexahydrate ($FeCl_3{\cdot}6H_2O$, 99.99%), and citric acid $C_8H_8O_7$ (99.5%) were purchased from Sigman Aldrich, and were used as starting materials for the synthesis of $MnFe_2O_4$/Carbon composite nano-powder and calcinated in an Argon (Ar) environment. The synthesized material was utilized to prepare the electrodes together with polyvinylidene fluoride (PVDF), 1-methyl-2-pyrrolidone (NMP), and

 doi:10.20944/preprints202602.1493.v1

conductive acetylene black (CAB). A 0.2 mm thick commercial nickel foam (NF) was sectioned into rectangular 1 × 3 cm^2 and circular 16 mm diameter pieces for three and two electrode configuration measurement, respectively then subjected to a chemical dip-washing process using 3 M hydrochloric acid (HCl), followed by acetone, and ethanol, with each solution dipped for 15 minutes before rinsed with deionized water (DI Water), and dried in an electric oven at 60 °C for 4 hrs [31].

2.2. Material Synthesis

MF/C nano powder was synthesized through the citrate sol-gel [32] and a calcination/carbonisation technique [19–21]. In summary, a solution was formulated using a 1:2 (Mn:Fe) ratio of metal ions and 1:1 ratio of metal ions to Citric Acid (CA), accomplished by dissolving 1.98 grams of $MnCl_2{\cdot}4H_2O$, 5.40 grams of $FeCl_3{\cdot}6H_2O$, and 5.76 grams of CA in 30 ml of DI Water. The CA served as a chelating agent ensuring metal ions separation and a source of carbon during the calcination/carbonisation process. The solution was continuously stirred in a magnetic stirrer at a constant temperature of 80 °C for 2 hours until the prepared solution turns into a gel, which was further dried in an oven at 100 °C for 3 hrs until a xerogel was obtained. The prepared xerogel was calcinated at 500 °C in a quartz tube furnace for 3 hrs in an Ar environment with a flow rate of 300 sccm (standard cubic centimetres per minute). The obtained powder was then crushed using a mortar and pestle. From a total precursor mass of 13.14 g, approximately 2.5 g of MF/C composite was obtained, corresponding to a yield of ~19%, with the mass loss mainly attributed to precursor decomposition, volatilization of organics, and chloride removal during carbonization. The preparation (synthesis) schematic is displayed in Figure 1.

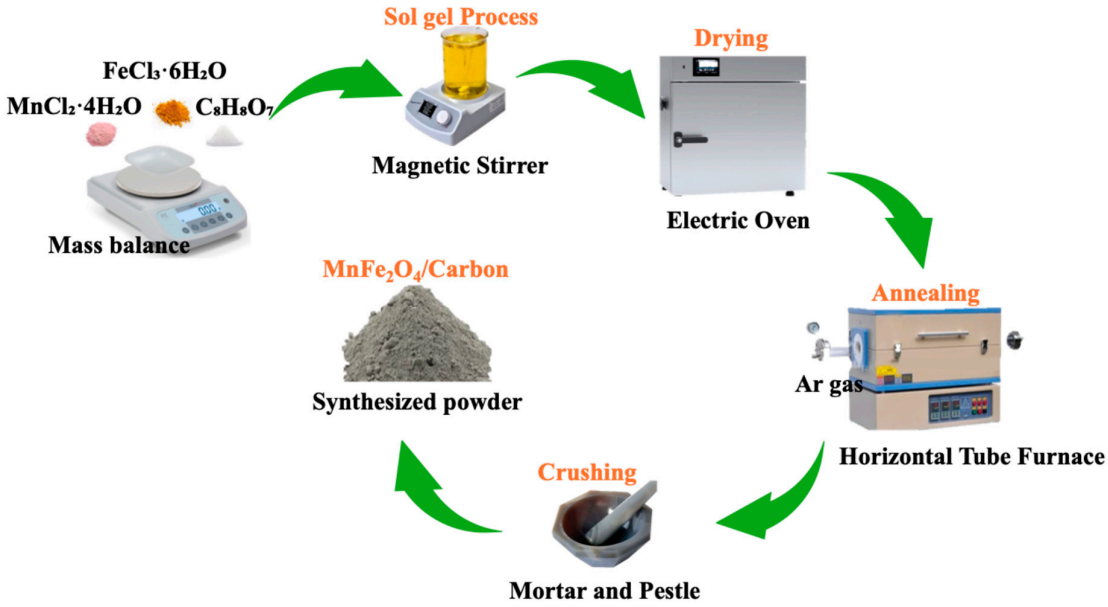

Figure 1. Schematic diagram illustrating the citrate sol – gel synthesis process of MF/C.

2.3. Characterisation

The Brucker 2D PAN analytical BV diffractometer (Amsterdam, Netherlands), equipped with CuKα (λ = 0.154 nm) over a 2θ range of 5 to 90°, was utilized to acquire X-ray diffraction patterns for assessing the crystallinity of the prepared material. The FTIR spectra of the materials were recorded in absorption mode using a Nicolet 750 FTIR spectrometer (Bruker). The nitrogen adsorption–desorption isotherms of MF/C were measured using a NOVA Touch NT 2LX-1 surface area and porosity analyzer (Quantachrome Instruments, Boynton Beach, Florida, USA), operated at 220 V and controlled by TouchWin software. The sample surfaces were degassed at 180 °C for 12 hours under

 doi:10.20944/preprints202602.1493.v1

vacuum to eliminate impurities and moisture. To study the specific surface areas of the adsorption branch, the Brunauer–Emmett–Teller (BET) method was used, operated in a relative pressure range (P/P0) of 0.01 to 0.2. In addition, density functional theory (DFT) method was used to calculate the pore size distributions from the desorption branch of the isotherms. The surface morphologies and elemental compositions of the material were studied using an energy dispersive spectrometer (EDS) coupled on a Zeiss Ultra Plus 55 Field Emission Scanning Electron Microscope (FE-SEM) (Carl Zeiss Microscopy GmbH, Oberkochen, Germany) running at an accelerating voltage of 20 kV and 2.0 kV, respectively.

2.4. Electrochemical Characterisation

All electrochemical analysis were conducted at room temperature using a Biologic VMP-300 potentiostat (Bio-Logic Science Instruments, Seyssinet-Pariset, France), controlled by EC-Lab software version V11.50. In the three-electrode system, a glassy carbon plate was used as the counter electrode, while an Ag/AgCl (with 3M KCl electrolyte inside) electrode functioned as the reference electrode. The working electrodes were fabricated by uniformly mixing the electroactive material (MF/C, 80 wt%) (wt% = weight percentage), conducting agent (CAB, 10 wt%), and binder (PVDF, 10 wt%), using NMP as a solvent, onto a piece of rectangular and circular NF. After coating, the electrode was dried overnight at 60 °C in an electric oven. The resulting mass-loading was determined and recorded in milligrams, ranging between 2.1 to 3.2 mg. Cyclic voltammetry (CV) was conducted at scan rates 5 – 1000 mVs^{-1} within an applied potential window of 0.0 – 0.4 V vs. Ag/AgCl. The galvanostatic charge/discharge (GCD) measurements were conducted at different specific current, which ranged from 1 to 5 Ag^{-1}. Electrochemical impedance spectroscopy (EIS) was performed in the frequency range of 100 kHz to 10 mHz with an amplitude of 10 mV at open circuit potential. Furthermore, the active material was electrochemically analysed using a two-electrode asymmetric device. In this device (MF/C//AC), MF/C served as the positive electrode, while AC derived from human hair served as the negative electrode. All electrochemical measurements for the three – and two – electrode configuration were carried out in a 3 M KOH aqueous electrolyte solution. Note that the negative electrode AC material was previously reported by our group [33,34], where it was analysed structurally and morphologically; and also tested for its supercapacitor capabilities.

3. Results and Discussion

3.1. Structural and Morphological

The powder-XRD analysis was utilized to examine the crystal structure and phase changes of the synthesized material. The powder XRD pattern of the MF/C is displayed in Figure 2a. The powder XRD pattern of the MF/C composite is displayed in Figure 2a, together with standard reference peaks of $MnFe_2O_4$ spinel (JCPDS no: 10-0319 [35]) The diffraction peaks were indexed to the face-centered cubic spinel structure of $MnFe_2O_4$ with space group $Fd\bar{3}m$, where Mn^{2+} and Fe^{3+} ions occupy the tetrahedral and octahedral sites, respectively. The indexed diffraction peaks correspond to the (220), (311), (400), (422), (511), and (440) crystallographic planes, confirming the formation of the $MnFe_2O_4$ spinel phase. No additional impurity peaks were observed, indicating high phase purity of $MnFe_2O_4$ in the MF/C composite [36]. The average crystallite size of $MnFe_2O_4$ was calculated using the Scherrer equation [37] applied to the most intense (311) diffraction peak, yielding a crystallite size of 12.5 nm, which is consistent with previously reported $MnFe_2O_4$ [38,39].

The FTIR spectrum of the MF/C composite shown in Figure 2b exhibits several characteristic absorption bands confirming the successful integration of carbon material with $MnFe_2O_4$ particles. The broad band centered at ~3448 cm^{-1} is attributed to O–H stretching vibrations, originating from surface hydroxyl groups. The weak band observed around 2450 cm^{-1} is associated with atmospheric CO_2 adsorption or overtone vibrations commonly observed in carbon-based materials. The absorption peak at ~1636 cm^{-1} corresponds to C=O stretching vibrations or H–O–H bending modes, indicating the presence of oxygen-containing functional groups on the carbon matrix. The band

 doi:10.20944/preprints202602.1493.v1

located at ~1356 cm^{-1} is assigned to C–O stretching vibrations, further confirming the presence of carbon–oxygen functional groups. While, the strong absorption band at ~556 cm^{-1} is characteristic of metal – oxygen (M–O–M) stretching vibrations within the $MnFe_2O_4$ spinel lattice, confirming the formation of the ferrite structure. These FTIR features are consistent with previously reported $MnFe_2O_4$, other spinel carbon-based composites and heteroatom – doped carbon materials, indicating successful bonding and interaction between $MnFe_2O_4$ nanoparticles and the carbon framework [39–41].

The unit cell structure of $MnFe_2O_4$ has been visualized using VESTA software (Ver. 3.5.2, 64-bit Edition) showing the position and bonding of Mn^{2+}, Fe^{3+} and O^{2-} within the $MnFe_2O_4$ structural matrix as shown in Figure 2c. The prepared material was taken for surface textural analysis and the obtained N_2 adsorption–desorption isotherms are displayed in Figure 2d. It reveals that the N_2 adsorption–desorption isotherm displays type-IV isotherms, which represent low-pressure monolayer adsorption and high-pressure multilayer adsorption [42]. Furthermore, the BET analysis estimated the average specific surface area of MF/C to be 29.62 m^2/g. Moreover, the material has a micropore surface area of 1.709 m^2/g and pore diameter of 2.65 nm. The pore size distribution in Figure 2e shows a small density of mesopores and micropores. The SEM micrographs presented in Figure 2f reveal agglomerated $MgAl_2O_4$ particles dispersed on the AC surface, exhibiting relatively large pore structures. The EDS spectrum and mapping are displayed on Figure S1 (Supplementary materials) and Figure 3, respectively, showing the presence of Manganese (Mn), Iron (Fe), oxygen (O), nitrogen (N), chlorine (Cl) and carbon (C) emanating from the precursor, while the carbon peak/concentration might have increased due to carbon tape during the SEM-EDS sample preparation. As shown in Figure 3, the elemental mapping reveals a relatively uniform distribution of all detected elements across the sample surface.

 doi:10.20944/preprints202602.1493.v1

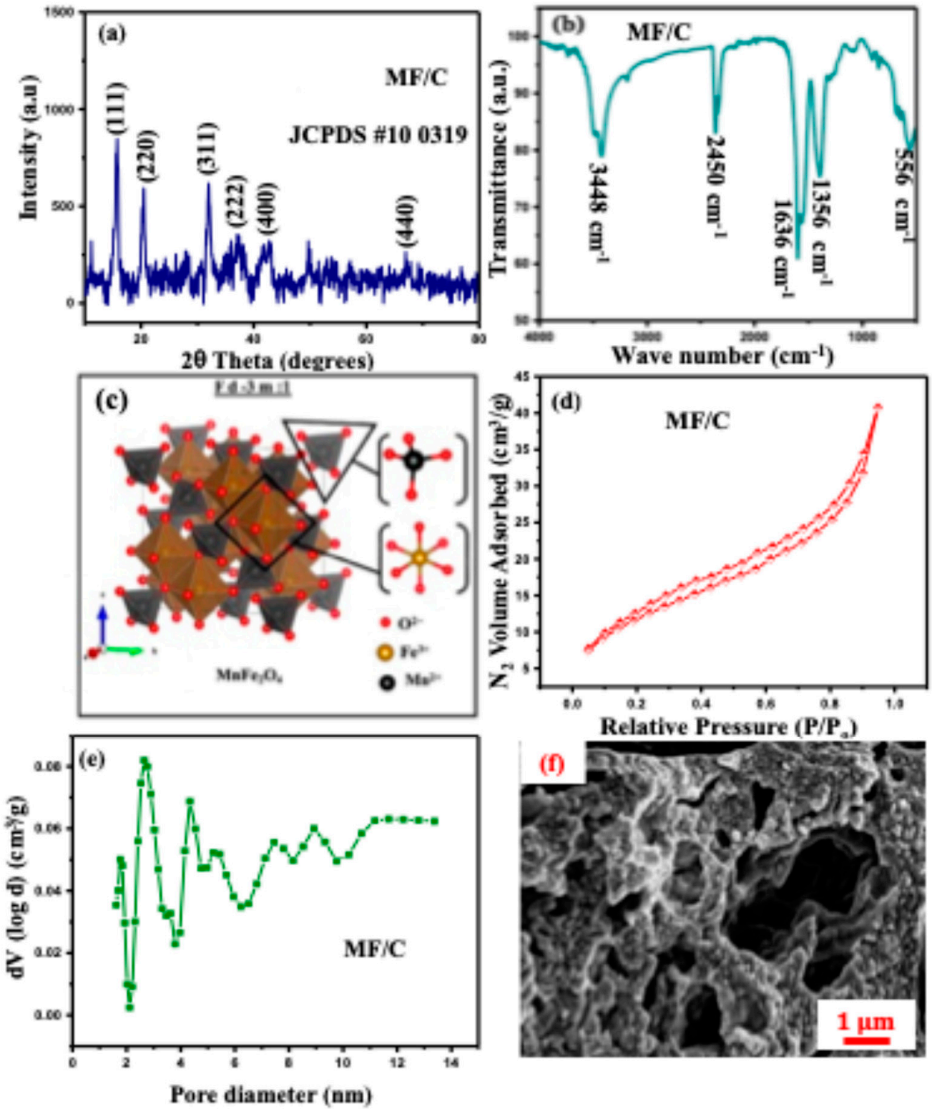

Figure 2. (a) X-ray diffraction, (b) FTIR spectrum, (c) unit cell, (d) N_2 adsorption/desorption isotherm, (e) Pore – size distribution, and (f) SEM micrographs of MF/C.

 doi:10.20944/preprints202602.1493.v1

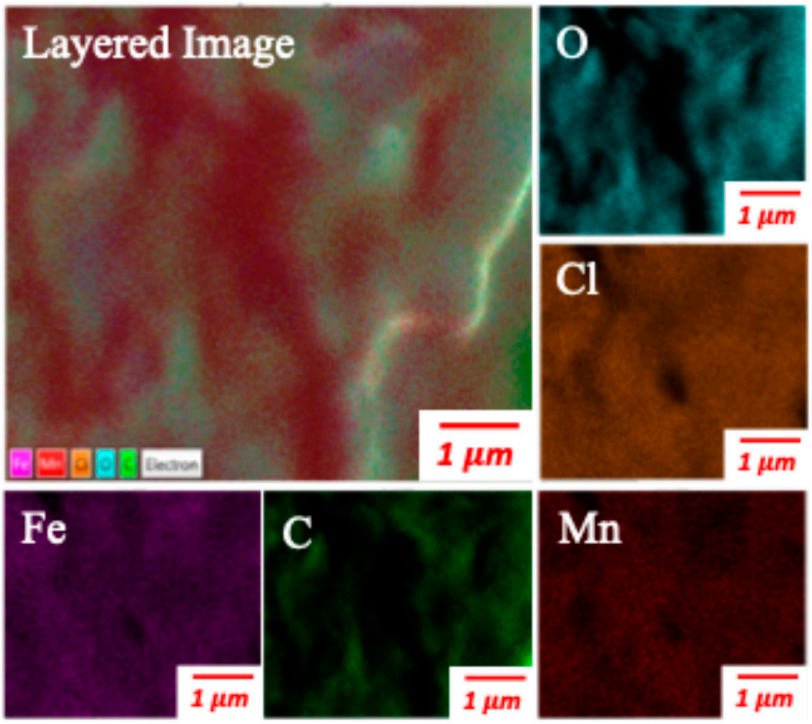

Figure 3. EDS mapping of MF/C.

3.2. Electrochemical Performance

Three-electrode configurations were employed to assess the electrochemical performance of the novel in-situ-prepared MF/C. The electrolyte was optimized by testing different KOH concentrations as shown in Figure S2, with 3 M KOH showing the best performance and subsequently being used throughout this entire study. The CV was performed at different scan rates ranging from 5 – 100 mVs^{-1} within a potential window of 0 – 0.4 vs Ag/AgCl, as shown in Figure 4a. The CV curves of MF/C exhibit prominent redox peaks, which signify quick redox reactions attributed to its pseudo-capacitive characteristics. The consistent observation of these redox peaks at all scan rates indicates a viable and reversible redox reaction [43] shown below on Equation (1) – (2):

$$MnFe_2O_4 + H_2O + OH^- \leftrightarrow MnOOH + 2FeOOH + e^- \quad (1)$$

$$FeOOH + OH^- \leftrightarrow FeO_2 + H_2O + e^- \quad (2)$$

With increasing scan rates, the oxidation peaks moved to higher potentials while the reduction peaks shifted to lower potentials. This happens because the electrolyte ions have limited time to access the electrode surface. This indicates that the oxidation and reduction reactions taking place during the process are quasi-reversible in nature [44]. The cyclic process undergoes extensive redox reactions as a result of polarization effects and ohmic resistance [7]. To better understand the charge storage mechanism, the relationship between peak current (i) and scan rate (ν) was analyzed using the power-law expression: $i = av^b$, where the b value indicates the dominant charge storage process. The b values calculated from the slope of log(i) versus log(ν) plots displayed in Figure S3, for the cathodic peaks were found to be 0.72 suggesting that the charge storage involves both surface-controlled capacitive processes and diffusion-controlled Faradaic reactions [45,46].

Figure 4b illustrates the GCD curve of the MF/C electrode at different specific currents within the potential range of 0 – 0.4 vs Ag/AgCl. All GCD curves exhibit a nonlinear characteristic with discharge plateaus, indicating the presence of Faradaic redox reactions as seen on the CV curves

 doi:10.20944/preprints202602.1493.v1

displayed in Figure 4a. The specific capacity (Q_s) in $mAhg^{-1}$ of the electrodes were calculated from the discharge curve of the GCD in Figure 4b using the Equation (3) [47]:

$$Q_s = \frac{I_s \times \Delta t}{3.6m} \quad (3)$$

where I_s represents the constant current (in amperes), Δt is the discharge time (in seconds), and m is the mass (in milligram) of the MF/C material. The GCD curves at a specific current of 1 A g^{-1} were used to determine the high specific capacity of 39.26 $mAhg^{-1}$, suggesting higher performance nature of the MF/C electrode. Figure 4c shows the rate capability of the MF/C active material showing a specific capacity retention of 69% at 5 Ag^{-1} of the initial 39.26 $mAhg^{-1}$. The reduction in specific capacity at high current density may be caused by the restricted access of OH^- ions to the internal active sites of the MF/C electrode, leading to incomplete redox reactions or time restrictions for redox reactions to occur. Moreover, slower diffusion rate of electrolyte ions into the electrode material also contributed to the decrease in capacity [43]. The EIS in Figure 4d was measured to further analyse the characteristic resistances and impedances of MF/C electrodes. The x-axis intercept corresponds to the equivalent series resistance (ESR), which is the total electrolyte resistance, inherent resistance of the electrode, and contact resistance between the current collector – electrode material – electrolyte. In the high-frequency range, the diameter of the semicircle represents the charge transfer resistance (R_{ct}) of the electrode, which is associated with the charge transfer processes at the electrode-electrolyte interface. The prepared sample showed an ESR and R_{ct} of 0.798 Ω and 2.5 Ω, respectively. In the low-frequency region, the 45° slanted line represents the Warburg impedance (W_s) of electrolyte diffusion, which is caused by the diffusion of ions from the electrolyte to the electrode surface [48]. The pseudocapacitive behaviour seen on the CV (Figure 4a), GCD (Figure 4b) curves and Nyquist plot (Figure 4d) is confirmed by the phase angle of $-61°$ displayed in Figure 4e of which falls within the range of $-45°$ to $-80°$ symbolising Faradaic behaviour.

 doi:10.20944/preprints202602.1493.v1

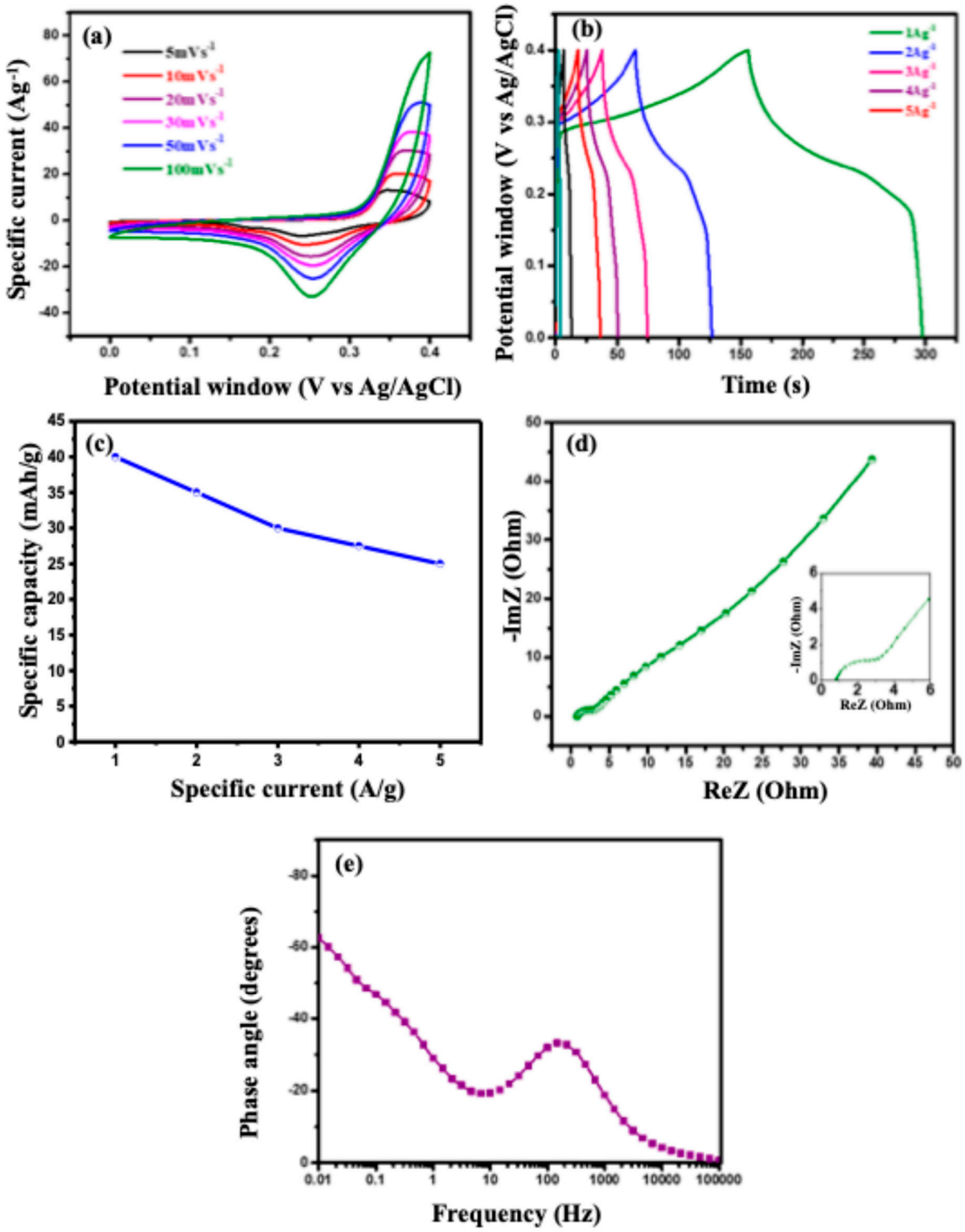

Figure 4. (a) CV curves at scan rates of 5 – 100 mVs^{-1}, (b) GCD curves at specific current ranging from 1 – 5 Ag^{-1}, (c) specific capacity versus specific current, (d) Nyquist plot, and (e) phase angle analysis of MF/C.

The Faradaic behaviour observed in Figure 4a,b, together with the material characterization results shown in Figures 2 and 3, suggests that $MnFe_2O_4$ nanoparticles are uniformly embedded and well-dispersed within the conductive carbon matrix, as illustrated in Figure 5. The carbonized carbon derived from citric acid provides abundant electric double-layer capacitance (EDLC) adsorption sites and forms a continuous conductive network that facilitates rapid electron transport throughout the electrode. In contrast, the $MnFe_2O_4$ nanoparticles act as Faradaic-active sites, contributing

 doi:10.20944/preprints202602.1493.v1

pseudocapacitance through reversible redox reactions. The intimate interfacial contact between $MnFe_2O_4$ and the carbon matrix shortens ion diffusion pathways and enables efficient electrolyte penetration into electroactive sites. Additionally, nitrogen and oxygen introduced via metal nitrate stabilizers result in heteroatom-doped carbon, which increases defect density and active sites while further improving electronic conductivity [49,50]. The presence of oxygen-containing functional groups enhances the hydrophilicity of the electrode surface, promoting improved wettability and faster ion transport at the electrode – electrolyte interface enhancing electrochemical performance of the MF/C composite[49].

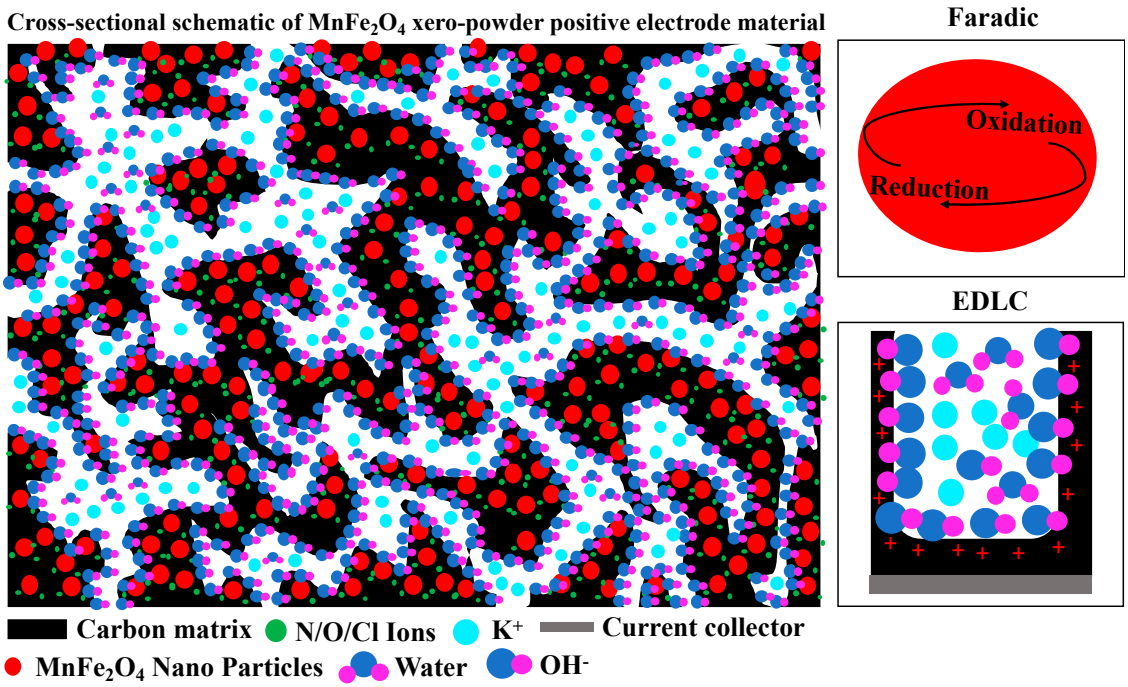

Figure 5. Cross sectional schematic of MF/C positive electroactive material.

To thoroughly evaluate the electrochemical performance of MF/C nano powder, a two – electrode asymmetric device was constructed, with MF/C as the positive and AC derived from human hair as the negative material [33,34]. The CV curves of the individual electrode materials, recorded within their respective potential windows, are presented in Figure 6a. As evident from the CV profiles, the AC electrode exhibits typical EDLC behaviour, characterized by a nearly rectangular shape, while the MF/C electrode demonstrates clear Faradaic features, indicating pseudocapacitive charge storage. The prepared device was then tested in 3M KOH electrolyte as they both perform optimally within that electrolyte. The charge disparity within the specific capacities/capacitance of the two electrodes was rectified by charge balance as described in equation S1 – S3 [51]. The MF/C//AC device exhibited a CV presented in Figure 6b measured at scan rates ranging from 5 mVs^{-1} to 1 Vs^{-1}, with a maximum voltage of 1.4 V which exceeds the combined potential window of 0.0 – 0.4 vs Ag/AgCl for MF/C and – 0.8 – 0.0 vs Ag/AgCl of AC due to the synergistic effect between the two electrode. The CV curves at different scan rates clearly show a combined contribution of EDLC from AC and Faradaic from $MnFe_2O_4$ behaviour, which is typical of a hybrid asymmetric supercapacitor. The GCD curves at different specific currents in the range of 1 – 5 A g^{-1} (Figure 6c) show potential steps, confirming the Faradaic behaviour of the device as indicated by the CV curves (Figure 6b). Since the device predominantly exhibits Faradaic behaviour, its specific capacity (Q_s) was determined from the GCD discharge curves using Equation (3) and was found to be 42.4 $mAhg^{-1}$ at a specific current of 1 Ag^{-1}. The rate capability curve displayed in Figure 6d shows a quick decay

 doi:10.20944/preprints202602.1493.v1

due to the above-mentioned reasons. Additionally, the specific energy (E_d in Wh kg^{-1}) and power density (P_d in W kg^{-1}) were determined from the GCD discharge curves using the following equations (4) and (5):

$$E_d = \frac{I_s}{3.6}\int_{Vi}^{Vf} V\,dt \tag{4}$$

$$P_d = \frac{E_d}{\Delta t}3600 \tag{5}$$

where I_s, Δt , and $\int_{Vi}^{Vf} V$ dt represent the specific current (Ag^{-1}), discharge time (s), and integral area under the curve of the GCD plot (Vs), respectively. The MF/C//AC hybrid device provided a specific energy and specific power as shown in Figure 6e where 1 Ag^{-1} shows a higher specific energy of 16.35 Wh kg^{-1} while the specific current of 5 Ag^{-1} showed a higher specific power of 1944.45 W kg^{-1}. The MF/C//AC device was assessed for material stability and degradation under constant CD for 15 000 cycles as displayed in Figure 6f. The material capacity retention (CR) of 92% of its initial capacity and columbic efficiency (n_c) of 99% [52].

$$\text{Capacity Retention (\%)} = \left(\frac{\text{Capacity at cycle n}}{\text{Initial Capacity}}\right) \times 100 \tag{6}$$

$$\text{n}_\text{c}\ (\%) = \left(\frac{\text{Q}_\text{discharge}}{\text{Q}_\text{charge}}\right) \times 100 \tag{7}$$

where Q is the charge? To further investigate the electrochemical behaviour of the device, including its conductivity and charge transport properties at the electrode/electrolyte interface, EIS was performed on the MF/C//AC asymmetric device see Figure 6g. The Nyquist plots display an ESR of 0.74Ω and the absence of a semicircle in the high-frequency range, while the low-frequency region shows a curve diverging away from the imaginary axis (y-axis), indicating voltage leakage. The maximum power, P_{max} of the device was estimated from Eq. (8)[51] below to be 236 kW kg^{-1}

$$P_{max} = \frac{\Delta V^2}{4m(ESR)} \tag{8}$$

where ΔV, m and ESR are the cell potential (V) of 1.4 V, mass of 2.8 ×10^{-6} kg and ESR of 0.74 Ω determined from the Nyquist plot in Figure 6g, respectively. The EIS fitting results presented as an inset in Figure 6g were obtained using the ZFIT module in EC-Lab software (version 11.50), employing the Randomise + Simplex fitting algorithm. The fitting quality was evaluated using optimized minimization parameters, including the chi-squared value (χ^2), its normalized form ($\chi/\sqrt{N}$), and the normalized chi-squared statistic ($\chi^2/|Z|^2$). As observed from the Nyquist plot in Figure 6g, there is no significant discrepancy between the experimental EIS data and the fitted equivalent circuit model. The equivalent circuit consists of a solution resistance (R_s) connected in series with a constant phase element (Q), which is arranged in parallel with the charge-transfer resistance (R_{CT}) and the Warburg diffusion element (W). The Warburg element, which governs ion diffusion from high- to low-frequency regions, is connected in series with R_{CT}. In an ideal scenario, a purely capacitive and perfectly polarizable electrode would exhibit a vertical line parallel to the imaginary axis at low frequencies, corresponding to the mass capacitance (C). However, the Nyquist plot in Figure 6g shows a deviation from this ideal capacitive behavior, which is attributed to the presence of a resistive component associated with the capacitance. This resistance is identified as the leakage resistance (R_L), connected in parallel with C. Figure 6h presents the Bode plot showing the impedance phase angle as a function of frequency for the MF/C//AC asymmetric device. The phase angle in the low-frequency region is approximately -50°, indicating Faradaic behaviour. Table 1 compares the electrochemical results obtained in this work with those found in previous studies that

 doi:10.20944/preprints202602.1493.v1

used Mn/Fe/carbon-based materials prepared via different synthesis techniques. Our device yields comparable results.

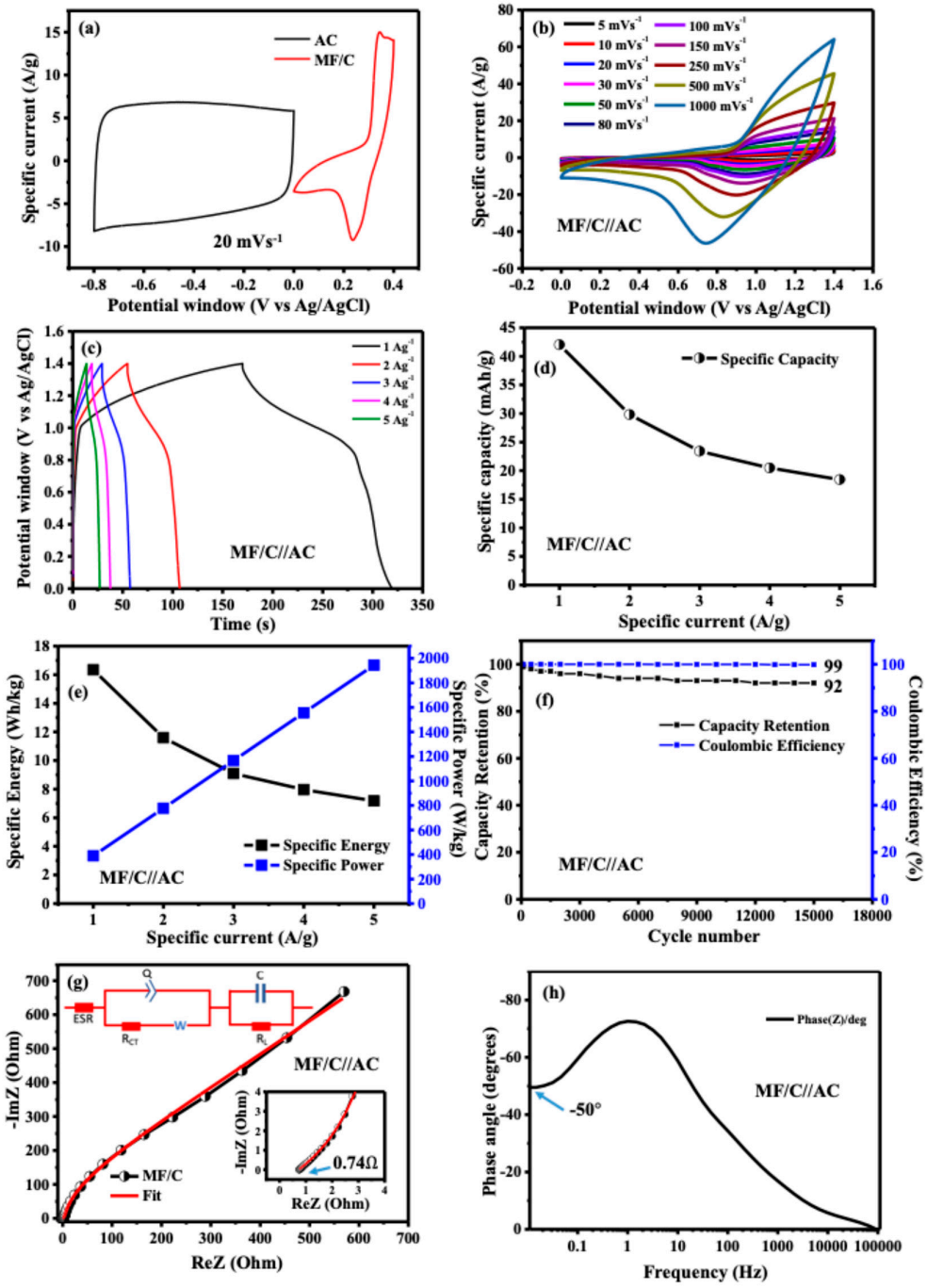

Figure 6. (a) CV curves of MF/C and AC electrodes recorded in the positive and negative potential windows, respectively; (b) CV curves of the MF/C//AC asymmetric device recorded at scan rates ranging from 5 to 1000 mV s^{-1}; (c) Galvanostatic charge–discharge (GCD) curves of the MF/C//AC device measured at specific currents from 1 to 10 A g^{-1}; (d) Specific capacity as a function of applied current density; (e) Specific energy and specific power as a function of applied current density; (f) Capacity retention and coulombic efficiency of the MF/C//AC device during cycling; (g) Nyquist plot of the MF/C//AC device (inset: enlarged high-frequency region) along with the fitted equivalent circuit; and (h) Phase angle analysis of the MF/C//AC device.

 doi:10.20944/preprints202602.1493.v1

Table 1. The electrochemical properties of supercapacitor devices prepared using different synthesis method with Mn/Fe/spinel/carbon-based composite materials. SPani ~ semi polycrystalline polyaniline; PANI ~ polyaniline; AC~ activated carbon and rGO ~ reduced graphene oxide.

Device	Method	Electrolyte	Cell voltage (Volt)	Cell capacitance (F g^{-1})	Specific energy (Whkg^{-1})	Specific power (Wkg^{-1})	Capacitance retention (%)/cycles number	Ref
SPani-AC//SPani-AC	Chemical polymerization	1M Na_2SO_4	1.5	45@ 5Ag-1	14	-	96/4500	[20]
Graphene/PANI	Electrochemical co-deposition polymerization	1M H_2SO_4	0.8	128 @ 0.5 A g^{-1}	11.38	199.8	85/10000	[53]
Mo-Doped $NiFe_2O_4$/NiF	sol-gel auto-combustion	1M KOH	0.5	268@1 A g^{-1}	20.55	567	-	[54]
Mn-$NiFe_2O_4$//AC	simple chemical etching and annealing treatment	1M KOH	1.5	1.726 @ 1 mA cm^{-2}	390 μWh cm^{-2}	544 μW cm^{-2}	95.2/5000	[55]
$MnFe_2O_4$@rGO//AC	Hydrothermal synthesis	1M KOH	0.55	325 @ 5 Ag^{-1}	11.8	540	75/10000	[14]
MF/C//AC	in situ citrate sol-gel and calcination method	3M KOH	1.4	42.4 mAhg^{-1}@ 1Ag^{-1}	16.35	1944.45	92/15000	This Work

4. Conclusions

In this research, MF/C was successfully synthesized using the in situ citrate sol-gel and calcination method. The structural and morphological analysis of the MF/C electrode revealed XRD peak corresponding to $MnFe_2O_4$. The FTIR analysis of the MF/C electrode exhibited characteristic absorption bands. The SEM images of $MnFe_2O_4$ reveal some fractured nanospheres, indicating the presence of hollow structures. The electrochemical performance of the MF/C working electrode was evaluated in a three-electrode cell setup with a 3M KOH electrolyte. Following this, an asymmetric device was successfully constructed using $MnFe_2O_4$ as the positive electrode and AC as the negative electrode. The $MnFe_2O_4$//AC asymmetric device that was fabricated demonstrated high performance at an applied potential difference of 1.4 V in 3M KOH. The device delivered a specific capacity of 42.4 mAh g^{-1}, a specific energy of 16.35 Wh kg^{-1}, and a maximum specific power of 236 kW kg^{-1}. Furthermore, it retained 92% of its capacitance after 15,000 charge–discharge cycles, confirming excellent long-term stability. Moreover, this work demonstrates an effective and low-cost synthesis route for MF/C composites, offering high electrochemical performance in both three – and two – electrode configuration, making it a promising electrode material for next – generation high – performance supercapacitor applications.

Supplementary Materials: The following supporting information can be downloaded at: https://www.mdpi.com/article/doi/s1, Figure S1: EDS spectra of $MnFe_2O_4$/Carbon; Figure S2: (a) CV Curves of $MnFe_2O_4$ at 20mVs^{-1}. (b) GCD Curves of MF/C at a current density of 1Ag^{-1}, (c) Electrochemical impedance spectroscopy (EIS) Nyquist plot of MF/C; Figure S3: The power law analysis of MF/C electrode material.

Author Contributions: Tshiamo Baloyi: Conceptualization, Methodology, Investigation, Data curation, Formal analysis, Writing original draft preparation. **Ndeye Fatou Diop:** Conceptualization, Data curation, Formal analysis, Writing – review & editing. **Rashed Ali Mohamed Adam:** Conceptualization, Data curation, Formal analysis, Writing – review & editing. **Erence Nkuna:** Formal analysis, Writing – review & editing. **Gift Rutavi:** Conceptualization, Formal analysis, Writing – review & editing. **Motlalepula Rebecca Mhlongo:** Resources, Writing – review & editing, Supervision, Funding acquisition. **Ncholu Manyala:** Conceptualization, Methodology, Resources, Writing – review & editing, Supervision, Project administration, Funding acquisition. **Vusani Muswa Maphiri:** Conceptualization, Methodology, Resources, Writing original draft preparation, Writing – review & editing, Supervision, Project administration, Funding acquisition.

 doi:10.20944/preprints202602.1493.v1

Funding: This research was funded by the National Research Foundation (NRF) of South Africa through the South African Research Chairs Initiative (SARChI) (Grant Number: RNESW24030772088354) and the Thuthuka Programme (Fund Number: TTK2205056950). Additional support was provided by the New Generation of Academics Programme (nGAP).

Data Availability Statement: The data will be available on request.

Acknowledgments: During the preparation of this manuscript/study, the author(s) used Microsoft bling for the purposes of to improve the readability. The authors have reviewed and edited the output and take full responsibility for the content of this publication. The authors thank Ms. Charity Maepa for her assistance with the morphological analysis.

Conflicts of Interest: The authors declare no conflict of interest.

References

1. S. Chai, R. Zheng, R. Guo, H. Luo, H. Cai, L. Liang, H. Huang, Z. Cheng, Manganese ferrite/reduced graphene oxide composites as energy storage electrode materials for supercapacitors, Ionics (Kiel). 30 (2024) 2957–2967. https://doi.org/10.1007/s11581-024-05477-6.
2. N.A. Althubiti, S. Aman, T.A.M. Taha, Synthesis of MnFe2O4/MXene/NF nanosized composite for supercapacitor application, Ceram. Int. 49 (2023) 27496–27505. https://doi.org/10.1016/j.ceramint.2023.06.025.
3. K. Malaie, M.R. Ganjali, Spinel nano-ferrites for aqueous supercapacitors; linking abundant resources and low-cost processes for sustainable energy storage, J. Energy Storage 33 (2021). https://doi.org/10.1016/j.est.2020.102097.
4. A. Manohar, V. Vijayakanth, S. V. Prabhakar Vattikuti, K.H. Kim, Synthesis and characterization of Mg2+ substituted MnFe2O4 nanoparticles for supercapacitor applications, Ceram. Int. 48 (2022) 30695–30703. https://doi.org/10.1016/j.ceramint.2022.07.018.
5. S.A.H. Moradi, N. Ghobadi, Fabrication of composite GO/NiFe2O4-MnFe2O4-CoFe2O4 anode material: Toward high performance hybrid supercapacitors, Microsc. Res. Tech. (2024) 1–16. https://doi.org/10.1002/jemt.24615.
6. S. Sharifi, K. Rahimi, A. Yazdani, Highly improved supercapacitance properties of MnFe2O4 nanoparticles by MoS2 nanosheets, Sci. Rep. 11 (2021) 1–15. https://doi.org/10.1038/s41598-021-87823-6.
7. H. Zhao, H. Jin, S. Li, Q. Tang, G. Sun, Q. Cheng, Y. Li, One-step rapid prototyping of recyclable ultrathin CNF/MWCNT/Fe-based spinel oxide asymmetric interdigital nanopaper electrodes for high performance flexible supercapacitors, Chemical Engineering Journal 498 (2024). https://doi.org/10.1016/j.cej.2024.155787.
8. A.N. Alqarni, E. Cevik, M.A. Gondal, M.A. Almessiere, A. Baykal, A. Bozkurt, Y. Slimani, M. Hassan, A. Iqbal, S.A. Alotaibi, Synthesis and design of vanadium intercalated spinal ferrite (Co0.5Ni0.5VxFe1.6−xO4) electrodes for high current supercapacitor applications, J. Energy Storage 51 (2022) 104357. https://doi.org/10.1016/j.est.2022.104357.
9. S. Sarr, D.T. Bakhoum, N.F. Sylla, N.M. Ndiaye, D.J. Tarimo, V.M. Maphiri, B.D. Ngom, N. Manyala, Enhancement of the electrochemical properties of vanadium dioxide via nitrogen-doped reduced graphene oxide for high-performance supercapacitor applications, New Journal of Chemistry 48 (2024) 13492–13505. https://doi.org/10.1039/d4nj01029a.
10. O.A. Akintayo, G.M. Al-Senani, S.A. Adewinbi, V.M. Maphiri, S.D. Al-Qahtani, N. Manyala, Boosting the pseudocapacitive response of spinel CoFe2O4 nanoparticles obtained by chemical hydrolysis via fine tuning their thermal-microstructural properties, Journal of Solid State Electrochemistry (2025). https://doi.org/10.1007/s10008-025-06378-y.
11. S.A. Adewinbi, V.M. Maphiri, L.O. Animasahun, M. Shkir, F.S. Khan, V.R. Minnam Reddy, S. Ganesh Moorthy, R. Marnadu, W.K. Kim, N. Manyala, Facile synthesis, enhanced annealing-structural investigation and supercapacitive potentials of NiFe2O4 spinel nanopowder, Surfaces and Interfaces 51 (2024). https://doi.org/10.1016/j.surfin.2024.104737.
12. S. Sharifi, K. Rahimi, A. Yazdani, Highly improved supercapacitance properties of MnFe2O4 nanoparticles by MoS2 nanosheets, Sci. Rep. 11 (2021). https://doi.org/10.1038/s41598-021-87823-6.

 doi:10.20944/preprints202602.1493.v1

13. Z.A. Jokandan, J. Mazloom, M.M. Ghaziani, Optimized electrospun MnFe2O4 nanofibers as promising electrode materials for supercapacitor applications: physical and electrochemical properties, Journal of Materials Science: Materials in Electronics 35 (2024). https://doi.org/10.1007/s10854-023-11918-1.
14. P. Sureka, G. Mahalakshmi, K. Vanasundari, N.K. Almulhem, M.W. Alam, Facile synthesis of nanoflower shaped MnFe2O4@rGO nanocomposite for ultra-stable asymmetric supercapacitor, Chem. Phys. Lett. 842 (2024). https://doi.org/10.1016/j.cplett.2024.141228.
15. M.M. Amini, M. Mirzaee, N. Sepanj, The effect of solution chemistry on the preparation of MgAl2O4 by hydrothermal-assisted sol-gel processing, Mater. Res. Bull. 42 (2007) 563–570. https://doi.org/10.1016/j.materresbull.2006.06.011.
16. X. Li, Q. Zha, Y. Ni, Ni-Fe Phosphate/Ni Foam Electrode: Facile Hydrothermal Synthesis and Ultralong Oxygen Evolution Reaction Durability, ACS Sustain. Chem. Eng. 7 (2019) 18332–18340. https://doi.org/10.1021/ACSSUSCHEMENG.9B03711/SUPPL_FILE/SC9B03711_SI_001.PDF.
17. J. Wang, F. Ren, B. Jia, X. Liu, Solvothermal synthesis and characterization of NiFe2O4 nanospheres with adjustable sizes, Solid State Commun. 150 (2010) 1141–1144. https://doi.org/10.1016/j.ssc.2010.03.021.
18. S.M. Mane, A.M. Teli, S.A. Beknalkar, J.C. Shin, J. Lee, Unveiling the Effect of Solution Concentration on the Optical and Supercapacitive Performance of CoWO4 Nanoparticles Prepared via the Solvothermal Method, Inorganics (Basel). 12 (2024). https://doi.org/10.3390/inorganics12080203.
19. M. Endo, T. Takeda, Y.J. Kim, K. Koshiba, K. Ishii, High Power Electric Double Layer Capacitor (EDLC ' s); from Operating Principle to Pore Size Control in Advanced Activated Carbons, Carbon Science 1 (2001) 117–128.
20. N. Mahato, T.V.M. Sreekanth, K. Yoo, J. Kim, Semi-Polycrystalline Polyaniline-Activated Carbon Composite for Supercapacitor Application, Molecules 28 (2023). https://doi.org/10.3390/molecules28041520.
21. E. Taer, A. Agustino, A. Fudholi, N. Chitraningrum, R. Taslim, High-performance symmetric supercapacitor based on activated carbon nanofibers derived from Napier grass fibers, Diam. Relat. Mater. 155 (2025). https://doi.org/10.1016/j.diamond.2025.112380.
22. V.M. Maphiri, D.T. Bakhoum, S. Sarr, N.F. Sylla, G. Rutavi, N. Manyala, Impact of Thermally Reducing Temperature on Graphene Oxide Thin Films and Microsupercapacitor Performance, Nanomaterials 12 (2022). https://doi.org/10.3390/nano12132211.
23. K. Thodkar, D. Thompson, F. Lüönd, L. Moser, F. Overney, L. Marot, C. Schönenberger, B. Jeanneret, M. Calame, Restoring the Electrical Properties of CVD Graphene via Physisorption of Molecular Adsorbates, ACS Appl. Mater. Interfaces 9 (2017) 25014–25022. https://doi.org/10.1021/acsami.7b05143.
24. M. Pedrosa, E.S. Da Silva, L.M. Pastrana-Martínez, G. Drazic, P. Falaras, J.L. Faria, J.L. Figueiredo, A.M.T. Silva, Hummers' and Brodie's graphene oxides as photocatalysts for phenol degradation, J. Colloid Interface Sci. 567 (2020) 243–255. https://doi.org/10.1016/j.jcis.2020.01.093.
25. S.N. Alam, N. Sharma, L. Kumar, Synthesis of Graphene Oxide (GO) by Modified Hummers Method and Its Thermal Reduction to Obtain Reduced Graphene Oxide (rGO)*, Graphene 06 (2017) 1–18. https://doi.org/10.4236/graphene.2017.61001.
26. M. Keshavarzi, G. Najafi, M. Salahshoor, M.H. Khoshtaghaza, S. Gorjian, H. Ghomi, A novel hybrid arc discharge–thermal method for sustainable brine treatment and resource recovery, Results in Engineering 27 (2025). https://doi.org/10.1016/j.rineng.2025.106521.
27. S. Sarr, N.F. Sylla, D.T. Bakhoum, N.M. Ndiaye, D.J. Tarimo, V.M. Maphiri, B.D. Ngom, N. Manyala, Vanadium dioxide sulphur-doped reduced graphene oxide composite as novel electrode material for electrochemical capacitor, J. Energy Storage 55 (2022). https://doi.org/10.1016/j.est.2022.105666.
28. O. Mondal, S. Mitra, M. Pal, A. Datta, S. Dhara, D. Chakravorty, Reduced graphene oxide synthesis by high energy ball milling, Mater. Chem. Phys. 161 (2015) 123–129. https://doi.org/10.1016/j.matchemphys.2015.05.023.
29. S.S. Patil, S.M. Mane, N.A. Nimbalkar, C.J. Khilare, S.B. Kulkarni, S.S. Dhasade, R.K. Kamat, J. Lee, S.G. Chavan, A simple facile synthesis for phase transforming of δ-MnO2 into α-MnO2 and thereby enhancing Na-ion supercapacitive performance, Ionics (Kiel). 30 (2024) 3055–3068. https://doi.org/10.1007/s11581-024-05458-9.

 doi:10.20944/preprints202602.1493.v1

30. S.M. Mane, A.M. Teli, S.A. Beknalkar, D.R. Patil, J.C. Shin, Cationic-Surfactant (CTAB) Assisted Preparation of 2D Graphitic Carbon Nitride (g-C3N4) Sheets Advances Supercapacitive Performance, Crystals (Basel). 14 (2024) 312. https://doi.org/10.3390/cryst14040312 (accessed February 8, 2026).
31. G. Rutavi, D.J. Tarimo, V.M. Maphiri, M. Ncholu, Two-step electrodeposition of Hausmannite sulphur reduced graphene oxide and cobalt-nickel layered double hydroxide heterostructure for high-performance supercapacitor, (2022) 1–14. https://doi.org/10.1002/er.7922.
32. A. Ahlawat, V.G. Sathe, V.R. Reddy, A. Gupta, Mossbauer, Raman and X-ray diffraction studies of superparamagnetic NiFe2O4 nanoparticles prepared by solgel auto-combustion method, J. Magn. Magn. Mater. 323 (2011) 2049–2054. https://doi.org/10.1016/j.jmmm.2011.03.017.
33. R.A.M. Adam, D.J. Tarimo, V.M. Maphiri, A.A. Mirghni, O. Fasakin, N. Manyala, Effects of the physisorption properties of human hair-derived activated carbon as a potential electrode for symmetric supercapacitor, Mater. Renew. Sustain. Energy 14 (2025). https://doi.org/10.1007/s40243-024-00294-3.
34. R.A.M. Adam, V.M. Maphiri, K.O. Otun, O. Fasakin, G. Rutavi, S. Thior, N. Manyala, Electropolymerization of polyaniline on coated activated carbon derived from human hair as a bilayer electrode for supercapacitor applications, J. Energy Storage 129 (2025). https://doi.org/10.1016/j.est.2025.117356.
35. L.P. Lingamdinne, V.R. Lebaka, J.R. Koduru, Y.Y. Chang, Insights into manganese ferrite anchored graphene oxide to remove Cd(II) and U(VI) via batch and semi-batch columns and its potential antibacterial applications, Chemosphere 310 (2023). https://doi.org/10.1016/j.chemosphere.2022.136888.
36. V. D'Ippolito, G.B. Andreozzi, D. Bersani, P.P. Lottici, Raman fingerprint of chromate, aluminate and ferrite spinels, Journal of Raman Spectroscopy 46 (2015) 1255–1264. https://doi.org/10.1002/jrs.4764.
37. V.Y. Zenou, S. Bakardjieva, Microstructural analysis of undoped and moderately Sc-doped TiO2 anatase nanoparticles using Scherrer equation and Debye function analysis, Mater. Charact. 144 (2018) 287–296. https://doi.org/10.1016/j.matchar.2018.07.022.
38. L.H. Nguyen, P.T.H. Tuyet, N.N.T. Linh, N.H. Du, L.T. Hung, P.H. Nam, D.T.T. Giang, L.T.T. Hiep, N.T. Suong, N.T. Tam, L.T. Hoa, L.T. Tam, Impact of surfactant concentration on applicability of MnFe2O4@poly(acrylic) acid nanoparticles in MRI and hyperthermia, Mater. Chem. Phys. 347 (2026). https://doi.org/10.1016/j.matchemphys.2025.131492.
39. H.M.A. Hassan, M.S. Alhumaimess, K. Alshammari, S.A. Al-Shammari, A.A. Barnawi, M.R. El-Aassar, Hydrothermal tailoring of MnFe2O4 nanospinel integrated with biodegradable polymers for improved CO oxidation efficiency, Colloids Surf. A Physicochem. Eng. Asp. 703 (2024). https://doi.org/10.1016/j.colsurfa.2024.135221.
40. M. Ebrahimi, M. Ghasemi, V. Soleimanian, M. Nekoeinia, A. Mokhtari, Effects of annealing temperature on microstructural, optical and FTIR properties of NiFe2O4 spinel nanoparticles, Chem. Phys. Lett. 833 (2023). https://doi.org/10.1016/j.cplett.2023.140911.
41. C. Dlamini, V.M. Maphiri, L.T. Melato, T.P. Mokoena, M.R. Mhlongo, Tuneable blue-green co-activated CaAl2O4: 0.1 mol% Tb3+, x mol% Sm3+ ($0 \leq x \leq 2$) nanophosphor prepared by citrate sol-gel method, Opt. Mater. (Amst). 142 (2023). https://doi.org/10.1016/j.optmat.2023.113985.
42. T. V. Tuyen, N.K. Chi, D.T. Tien, N. Tu, N. V. Quang, P.T.L. Huong, Carbon-encapsulated MnFe2O4 nanoparticles: effects of carbon on structure, magnetic properties and Cr(VI) removal efficiency, Appl. Phys. A Mater. Sci. Process. 126 (2020) 1–12. https://doi.org/10.1007/s00339-020-03760-7.
43. Z.A. Jokandan, J. Mazloom, M.M. Ghaziani, Optimized electrospun MnFe2O4 nanofibers as promising electrode materials for supercapacitor applications: physical and electrochemical properties, Journal of Materials Science: Materials in Electronics 35 (2024) 1–15. https://doi.org/10.1007/s10854-023-11918-1.
44. E.C. Silva, P.J. Zambiazi, T.V.B. Ferraz, J.A. Bonacin, R.R. Passos, L.A. Pocrifka, Modulating the electrochemical capacitance of NiFe2O4 by an external magnetic field for energy storage application, Journal of Electroanalytical Chemistry 901 (2021) 115758. https://doi.org/10.1016/j.jelechem.2021.115758.
45. R. Cheruku, D.S. Bhaskaram, G. Govindaraj, Variable range hopping and relaxation mechanism in graphene oxide sheets containing sp3 hybridization induced localization, Journal of Materials Science: Materials in Electronics 29 (2018) 9663–9672. https://doi.org/10.1007/s10854-018-9003-6.

 doi:10.20944/preprints202602.1493.v1

46. J. Sun, X. Yu, S. Zhao, H. Chen, K. Tao, L. Han, Solvent-Controlled Morphology of Amino-Functionalized Bimetal Metal-Organic Frameworks for Asymmetric Supercapacitors, Inorg. Chem. 59 (2020) 11385–11395. https://doi.org/10.1021/acs.inorgchem.0c01157.
47. M.N. Rantho, M.J. Madito, N. Manyala, High-performance symmetric supercapacitor device based on carbonized iron-polyaniline/nickel graphene foam, J. Alloys Compd. 819 (2020) 1–33. https://doi.org/10.1016/j.jallcom.2019.152993.
48. M.N. Rantho, M.J. Madito, F.O. Ochai-Ejeh, N. Manyala, Asymmetric supercapacitor based on vanadium disulfide nanosheets as a cathode and carbonized iron cations adsorbed onto polyaniline as an anode, Electrochim. Acta 260 (2018) 11–23. https://doi.org/10.1016/j.electacta.2017.11.074.
49. Q. Zhang, Y. Xin, H. Qin, Z. Xu, Y. Chen, S. Wang, Nitrogen/oxygen dual-doped hierarchical porous carbons with inverse opal-like structure for high performance supercapacitors, J. Alloys Compd. 900 (2022). https://doi.org/10.1016/j.jallcom.2021.163537.
50. S. Jiang, Y. Sun, H. Dai, J. Hu, P. Ni, Y. Wang, Z. Li, Facile synthesis of nitrogen and sulfur dual-doped hierarchical micro/mesoporous carbon foams as efficient metal-free electrocatalysts for oxygen reduction reaction, Electrochim. Acta 174 (2015) 826–836. https://doi.org/10.1016/j.electacta.2015.06.050.
51. V.M. Maphiri, D.T. Bakhoum, S. Sarr, N.F. Sylla, G. Rutavi, N. Manyala, Low temperature thermally reduced graphene oxide directly on Ni-Foam using atmospheric pressure-chemical vapour deposition for high performance supercapacitor application, J. Energy Storage 52 (2022) 104967. https://doi.org/10.1016/j.est.2022.104967.
52. D.T. Bakhoum, N.F. Sylla, S. Sarr, V.M. Maphiri, N.M. Ndiaye, D.J. Tarimo, A. Seck, B.D. Ngom, M. Chaker, N. Manyala, Nitrogen-phosphorous co-doped porous carbon from cross-linked polymers for supercapacitor applications, J. Energy Storage 68 (2023). https://doi.org/10.1016/j.est.2023.107695.
53. L. Wen, K. Li, J. Liu, Y. Huang, F. Bu, B. Zhao, Y. Xu, Graphene/polyaniline@carbon cloth composite as a high-performance flexible supercapacitor electrode prepared by a one-step electrochemical co-deposition method, RSC Adv. 7 (2017) 7688–7693. https://doi.org/10.1039/c6ra27545a.
54. N. Chaudhari, S.K. Jagadale, R. Patil, P. Dusane, Y. More, M. Kute, P. Bankar, S.M. Rathod, "Nanostructured Mo- Doped NiFe2O4: A Promising Electrode Materials for Supercapacitor with Improved Charge Storage Capacity," Solid State Sci. (2025) 108033. https://doi.org/10.1016/j.solidstatesciences.2025.108033.
55. K. Yan, R. Chen, Q. Ling, Z. Zhao, Z. Zhou, X. Li, J. Lv, C. Cao, G. He, Z. Sun, M. Zhang, Rapid synthesis of Mn-doped NiFe2O4 nanosheet arrays for high-performance hybrid supercapacitors, Electrochim. Acta 497 (2024). https://doi.org/10.1016/j.electacta.2024.144551.